Supplementary Material for

Geometry-locked acoustic orbital polarization enables switchable bound states in the continuum

Zeliang Song[1], Quansen Wang[2], Yong Li[2,*] and Degang Zhao[1,†]

1 Department of Physics, Huazhong University of Science and Technology, Wuhan 430074, China.

2 Institute of Acoustics, School of Physics Science and Engineering, Tongji University, Shanghai 200092, China.

* Corresponding author. E-mail: yongli@tongji.edu.cn

† Corresponding author. E-mail: dgzhao@hust.edu.cn

This file includes:

P1. Analytical derivation of modal degeneracy lifting in an SWG.

We start from a simple circular waveguide (CWG) with radius r_0, as Fig. S1(a) shows. The in-plane (dropping z component) wave equation with hard boundary condition is

$$\left(\nabla_t^2 + k_{mn}^2\right)\alpha = 0,\ \left.\frac{\partial\alpha}{\partial r}\right|_{r=r_0} = 0, \tag{S1}$$

where $\nabla_t^2 = \frac{1}{r}\frac{\partial}{\partial r}\left(r\frac{\partial}{\partial r}\right) + \frac{1}{r^2}\frac{\partial^2}{\partial\varphi^2}$ is the transverse component of the Laplacian in polar coordinates.

When $m > 0$, a pair of degenerate eigensolutions can be expressed as

$$\begin{aligned} \alpha_1(r,\varphi) &= \frac{1}{\sqrt{N_{mn}}} J_m(k_{mn}r)\cos m\varphi \\ \alpha_2(r,\varphi) &= \frac{1}{\sqrt{N_{mn}}} J_m(k_{mn}r)\sin m\varphi \end{aligned}, \tag{S2}$$

where $J_m(k_{mn}r)$ is the Bessel function of the first kind of mth order, k_{mn} is the in-plane wavenumber, which is the n-th root of $\left.\frac{\mathrm{d}J_m(k_{mn}r)}{\mathrm{d}r}\right|_{r=r_0} = 0$. N_{mn} is the normalized coefficient. We can formally write the Hamiltonian equation for the CWG as

$$\begin{aligned} \hat{H}_0\alpha_1 &= k_{mn}^2\alpha_1 \\ \hat{H}_0\alpha_2 &= k_{mn}^2\alpha_2 \end{aligned}, \tag{S3}$$

where $\hat{H}_0 = -\nabla_t^2$, denoting the unperturbed operator. Note that here the physical observable corresponding to this operator is the square of the in-plane wavenumber. Since these two eigensolutions are orthogonal in Hilbert space, we harness the column vector to represent the states in Eq. (S2). We use the Dirac notations to represent them as $|\alpha_1\rangle = [1\quad 0]^T, |\alpha_2\rangle = [0\quad 1]^T$. The Hamiltonian H_0 can be thereby diagonalized as

$$H_0 = \begin{pmatrix} \langle\alpha_1|\hat{H}_0|\alpha_1\rangle & \langle\alpha_1|\hat{H}_0|\alpha_2\rangle \\ \langle\alpha_2|\hat{H}_0|\alpha_1\rangle & \langle\alpha_2|\hat{H}_0|\alpha_2\rangle \end{pmatrix} = \begin{pmatrix} k_{mn}^2 & 0 \\ 0 & k_{mn}^2 \end{pmatrix}. \tag{S4}$$

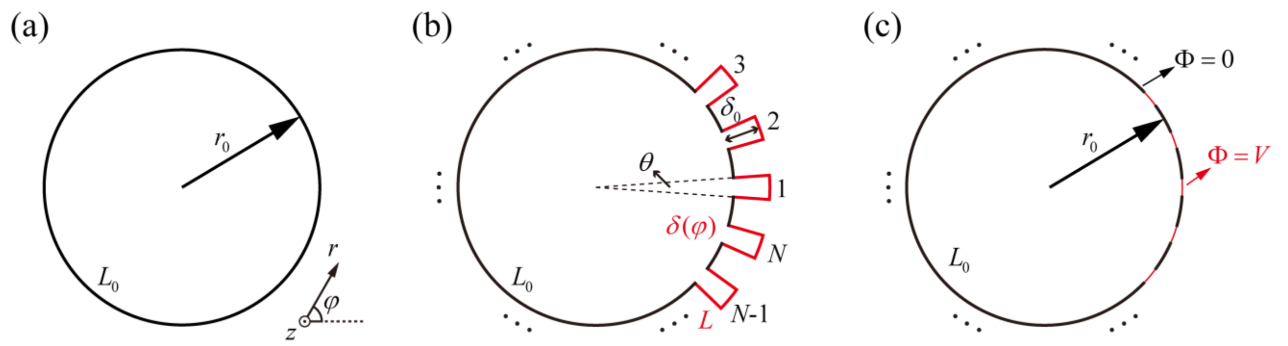

Fig. S1 Schematic diagram of the effective-potential perturbation in an SWG. (a) Scheme of CWG. (b) Scheme of SWG. Equidistantly distributed sawtooth grooves on the boundary can be viewed as a slight radial-shift perturbation δ_0 of a CWG's boundary L_0, forming a sawtoothed boundary L. N is the number of sawtooth convex. θ is the central angle of each convex. (c) Equivalent model for SWG. The convex grooves bring nonzero reflection phase on the circular boundary L_0, exerting a periodic perturbation operator V.

Next, we consider a waveguide with sawtoothed boundary (SWG) as a perturbed system. An SWG is constructed as follows: part of the hard boundary of a CWG is radially extended for a short distance δ_0, as shown in Fig. S1(b), forming a C_N-symmetric boundary with periodically distributed sawtooth features. The prolongation of the boundary can be described as a function

$$\delta(\varphi)=\begin{cases}\delta_0, & \dfrac{2\pi(i-1)}{N}-\dfrac{\theta}{2}<\varphi<\dfrac{2\pi(i-1)}{N}+\dfrac{\theta}{2}(i=1,2,\ldots,N) \\ 0, & \text{otherwise}\end{cases}, \tag{S5}$$

where θ is the central angle of each convex. Here δ_0 is set to be much smaller than r_0 and thus it can be considered as a perturbation. Apparently, owing to the convex, the circular boundary L_0 is no longer a perfectly rigid wall. Instead, the convex plays the role of metasurface that results in nonzero reflection phase on the boundary [1]. The total Hamiltonian operator for the on-boundary eigensolution in the SWG can be expressed as

$$H = H_0 + V, \tag{S6}$$

and the corresponding eigenequation is

$$H\left|\beta\right\rangle = \left(H_0 + V\right)\left|\beta\right\rangle = k_r^2\left|\beta\right\rangle, \tag{S7}$$

where $\left|\beta\right\rangle$ is the perturbed eigenstate with respect to $\hat{H}$, corresponding to eigenvalue k_r^2. To the first-order approximation, the perturbation operator is defined by $V = \delta(\varphi)\dfrac{\partial^2}{\partial r^2}$ (The proof of this form associated with the approximation will be provided in the following content). The perturbation operator V exerting on the CWG boundary resembles a periodic scattering potential, mimicking the classical Stark effect for an atomic electron in a static electric field.

Under the perturbation of the sawtooth grooves, the in-plane wave equation becomes

$$\left(\nabla_t^2 + k_r^2\right)\beta = 0, \left.\frac{\partial\beta}{\partial r}\right|_{r=r_0+\delta(\varphi)} = 0, \tag{S8}$$

where k_r is the effective in-plane wavenumber corresponding to the perturbed eigenstate $\beta(r,\varphi)$. β can be reasonably written as the linear superposition of the basis α_1 and α_2

$$\beta = C_1\alpha_1 + C_2\alpha_2, \tag{S9}$$

where C_1 and C_2 are undetermined coefficients. Here Eq. (S9) is valid only when the bias between L_0 and L, i.e. δ_0, is much smaller than the in-plane wavelength. So, we can write Taylor-series expansion of $\left.\dfrac{\partial\beta}{\partial r}\right|_{r=r_0+\delta(\varphi)}$

$$0 = \left.\frac{\partial\beta}{\partial r}\right|_{r=r_0+\delta(\varphi)} = \left.\frac{\partial\beta}{\partial r}\right|_{r=r_0} + \delta(\varphi)\left.\frac{\partial^2\beta}{\partial r^2}\right|_{r=r_0} + \dots. \tag{S10}$$

Substituting Eq. (S9) into Eq. (S10) and neglecting the high-order small quantities, we have

$$\left.\frac{\partial\beta}{\partial r}\right|_{r=r_0} = -\delta(\varphi)\left(C_1\left.\frac{\partial^2\alpha_1}{\partial r^2}\right|_{r=r_0} + C_2\left.\frac{\partial^2\alpha_2}{\partial r^2}\right|_{r=r_0}\right). \tag{S11}$$

Rewrite the wave equation for β

$$\left(\nabla_t^2 + k_r^2\right)\beta = 0, \left.\frac{\partial\beta}{\partial r}\right|_{r=r_0} = -\delta(\varphi)\left(C_1\left.\frac{\partial^2\alpha_1}{\partial r^2}\right|_{r=r_0} + C_2\left.\frac{\partial^2\alpha_2}{\partial r^2}\right|_{r=r_0}\right). \tag{S12}$$

Left-multiply the conjugate form of equation $\left(\nabla_t^2 + k_{mn}^2\right)\alpha_1 = 0$ by β and Eq. (S12) by α_1^*, integrating over the in-plane area, we obtain

$$\iint_{S_0} \left(\beta \nabla_t^2 \alpha_1^* - \alpha_1^* \nabla_t^2 \beta\right) \mathrm{d}s = \left(k_r^2 - k_{mn}^2\right) \iint_{S_0} \beta \alpha_1^* \mathrm{d}s, \tag{S13}$$

where S_0 represents the area enclosed by L_0. Apply Green's 2nd identity and use Eq. (S11), we have

$$\oint_{L_0} \delta(\varphi) \left(\alpha_1^* C_1 \frac{\partial^2 \alpha_1}{\partial r^2} + \alpha_1^* C_2 \frac{\partial^2 \alpha_2}{\partial r^2} \right) \mathrm{d}l = \left(k_r{}^2 - k_{mn}{}^2\right) C_1. \tag{S14}$$

Likewise, we perform the same operation on equation $\left(\nabla_t^2 + k_{mn}^2\right)\alpha_2 = 0$

$$\oint_{L_0} \delta(\varphi) \left(\alpha_2^* C_1 \frac{\partial^2 \alpha_1}{\partial r^2} + \alpha_2^* C_2 \frac{\partial^2 \alpha_2}{\partial r^2} \right) \mathrm{d}l = \left(k_r{}^2 - k_{mn}{}^2\right) C_2. \tag{S15}$$

Eqs. (S14) and (S15) have composed an eigenvalue equation, which is expressed as

$$V \begin{pmatrix} C_1 \\ C_2 \end{pmatrix} = \left(k_r^2 - k_{mn}^2\right) \begin{pmatrix} C_1 \\ C_2 \end{pmatrix}, \tag{S16}$$

where V is the operator of the sawtooth perturbation whose expression under the basis α_1 and α_2 is

$$V = \begin{pmatrix} \oint_{L_0} \alpha_1^* \delta(\varphi) \frac{\partial^2 \alpha_1}{\partial r^2} \mathrm{d}l & \oint_{L_0} \alpha_1^* \delta(\varphi) \frac{\partial^2 \alpha_2}{\partial r^2} \mathrm{d}l \\ \oint_{L_0} \alpha_2^* \delta(\varphi) \frac{\partial^2 \alpha_1}{\partial r^2} \mathrm{d}l & \oint_{L_0} \alpha_2^* \delta(\varphi) \frac{\partial^2 \alpha_2}{\partial r^2} \mathrm{d}l \end{pmatrix}. \tag{S17}$$

Next, we substitute Eq. (S5) into Eq. (S17). Note that $\oint_{L_0} \mathrm{d}l = r_0 \int_0^{2\pi} \mathrm{d}\varphi$. It yields

$$
\begin{aligned}
V &= \delta_0 \frac{R_{mn}}{N_{mn}} \begin{bmatrix} \int_0^{2\pi} \mathrm{d}\varphi \cos m\varphi \delta(\varphi) \cos m\varphi & \int_0^{2\pi} \mathrm{d}\varphi \cos m\varphi \delta(\varphi) \sin m\varphi \\ \int_0^{2\pi} \mathrm{d}\varphi \sin m\varphi \delta(\varphi) \cos m\varphi & \int_0^{2\pi} \mathrm{d}\varphi \sin m\varphi \delta(\varphi) \sin m\varphi \end{bmatrix} \\
&= \delta_0 \frac{R_{mn}}{N_{mn}} \begin{bmatrix} \sum_{i=1}^{N} \left[\frac{\theta}{2} + \frac{1}{2m} \cos \frac{(i-1)4m\pi}{N} \sin m\theta \right] & \sum_{i=1}^{N} \frac{1}{2m} \sin \frac{(i-1)4m\pi}{N} \sin m\theta \\ \sum_{i=1}^{N} \frac{1}{2m} \sin \frac{(i-1)4m\pi}{N} \sin m\theta & \sum_{i=1}^{N} \left[\frac{\theta}{2} - \frac{1}{2m} \cos \frac{(i-1)4m\pi}{N} \sin m\theta \right] \end{bmatrix} \\
&= \delta_0 \frac{R_{mn}}{N_{mn}} \begin{bmatrix} \frac{N\theta}{2} + \frac{\sin m\theta}{2m} \sum_{i=1}^{N} \cos \frac{(i-1)4m\pi}{N} & \frac{\sin m\theta}{2m} \sum_{i=1}^{N} \sin \frac{(i-1)4m\pi}{N} \\ \frac{\sin m\theta}{2m} \sum_{i=1}^{N} \sin \frac{(i-1)4m\pi}{N} & \frac{N\theta}{2} - \frac{\sin m\theta}{2m} \sum_{i=1}^{N} \cos \frac{(i-1)4m\pi}{N} \end{bmatrix} \\
&= \begin{cases} \begin{bmatrix} \frac{N\theta\delta_0}{2} \frac{R_{mn}}{N_{mn}} \left(1 + \frac{\sin m\theta}{m\theta} \right) & 0 \\ 0 & \frac{N\theta\delta_0}{2} \frac{R_{mn}}{N_{mn}} \left(1 - \frac{\sin m\theta}{m\theta} \right) \end{bmatrix}, \text{ if } \frac{2m}{N} \in \mathbb{Z} \\ \frac{N\theta\delta_0}{2} \frac{R_{mn}}{N_{mn}} \begin{bmatrix} 1 & 0 \\ 0 & 1 \end{bmatrix} \qquad ,\text{if } \frac{2m}{N} \notin \mathbb{Z} \end{cases}
\end{aligned}
, \qquad \text{(S18)}
$$

where $R_{mn} = r_0 J_m(k_{mn} r_0) \left[\frac{\partial^2 J_m(k_{mn} r)}{\partial r^2} \right]_{r=r_0}$. The final step of Eq. (S18) is obtained in terms of

$$
\begin{aligned}
&\sum_{i=1}^{N} \cos \frac{(i-1)4m\pi}{N} = \begin{cases} N, & \text{if } \frac{2m}{N} \in \mathbb{Z} \\ \mathrm{Re}\left(\sum_{i=1}^{N} e^{j\frac{(i-1)4m\pi}{N}} \right) = \mathrm{Re}\left(\frac{1-e^{j4m\pi}}{1-e^{j\frac{4m\pi}{N}}} \right) = 0, & \text{if } \frac{2m}{N} \notin \mathbb{Z} \end{cases} . \\
&\sum_{i=1}^{N} \sin \frac{(i-1)4m\pi}{N} \equiv 0
\end{aligned}
\qquad \text{(S19)}
$$

According to Eq. (S17) and Eq. (S18), we can solve k_r and rewrite it into $k_{mn,\pm}$, referring to the perturbed cutoff wavenumbers for (m,n)-th order eigenmodes, given by

$$
k_{mn,\pm}^2 - k_{mn}^2 = \begin{cases} \frac{N\theta\delta_0}{2} \frac{R_{mn}}{N_{mn}} \left(1 \pm \frac{\sin m\theta}{m\theta} \right), & \text{if } \frac{2m}{N} \in \mathbb{Z} \\ \frac{N\theta\delta_0}{2} \frac{R_{mn}}{N_{mn}}, & \text{if } \frac{2m}{N} \notin \mathbb{Z} \end{cases} . \qquad \text{(S20)}
$$

Apparently, Eq. (S20) indicates $\frac{2m}{N} \in \mathbb{Z}$ is the prerequisite condition for degeneracy lifting. And within it, there is a special situation when $m\theta = \pi\mathbb{Z}$, the degeneracy of the previously split eigenmodes will be restored.

Eventually, one obtains the two essential conditions for the lifting of eigenmodes in SWG, which are

$$\begin{aligned} &\text{Condition } 1: \frac{2m}{N} \in \mathbb{Z}; \\ &\text{Condition } 2: m\theta \notin \pi\mathbb{Z}. \end{aligned} \tag{S21}$$

When Condition 1 and Condition 2 are both satisfied, the cutoff frequencies of degeneracy lifted eigenmodes are

$$f_{\pm} = \frac{ck_{mn,\pm}}{2\pi} = \frac{c}{2\pi}\sqrt{k_{mn}^2 + \frac{N\theta\delta_0}{2}\frac{R_{mn}}{N_{mn}}\left(1 \pm \frac{\sin m\theta}{m\theta}\right)}. \tag{S22}$$

If one of (or both) Condition 1 and Condition 2 is not satisfied, the cutoff frequency of degenerate eigenmodes is

$$f_{+} = f_{-} = \frac{c}{2\pi}\sqrt{k_{mn}^2 + \frac{N\theta\delta_0}{2}\frac{R_{mn}}{N_{mn}}}. \tag{S23}$$

Although the eigenmodes remain degenerate, their cutoff frequencies are different from that in CWG owing to the wave scattering by the sawtooth boundary. These essential conditions point out a clear path to lift the degeneracy of a certain $m > 0$ eigenmode, that the number of sawtooth grooves (N) and the size of each single sawtooth (θ) should be reasonably designed.

We verify the analytical formula of the cutoff frequencies [Eqs. (S22) and (S23)] by comparing them with the simulation results. Table 1 records the analytically calculated and numerically simulated cutoff frequencies for all $m > 0$ eigenmodes corresponding to Fig. 2(f) in the main text. They match very well, as the greatest relative error is only 1.89%.

Mode	(1,0)			(2,0)			(3,0)			(4,0)			(1,1)		
N	Freq (Hz)		Rel. Err.	Freq (Hz)		Rel. Err.	Freq (Hz)		Rel. Err.	Freq (Hz)		Rel. Err.	Freq (Hz)		Rel. Err.
	Sim.	Theo.		Sim.	Theo.		Sim.	Theo.		Sim.	Theo.		Sim.	Theo.	
1	2538.9	2542.3	0.14%	4207.0	4217.3	0.24%	5781.7	5800.9	0.33%	7291.3	7342.5	0.70%	7377.0	7362.2	-0.20%
	2550.8	2549.4	-0.05%	4233.0	4228.9	-0.10%	5824.5	5816.8	-0.13%	7373.8	7362.1	-0.16%	7382.9	7382.1	-0.01%
2	2528.6	2535.3	0.26%	4185.2	4205.4	0.48%	5745.1	5784.6	0.69%	7259.0	7322.0	0.87%	7332.4	7342.1	0.13%
	2552.1	2549.4	-0.11%	4237.1	4228.8	-0.20%	5832.0	5816.4	-0.27%	7385.7	7361.3	-0.33%	7382.8	7382.1	-0.01%
3	2535.6	2538.8	0.12%	4202.6	4211.2	0.20%	5718.0	5768.3	0.88%	7262.9	7331.0	0.94%	7379.2	7352.1	-0.37%
							5839.4	5816.0	-0.40%						
4	2531.3	2535.2	0.16%	4143.7	4181.7	0.92%	5759.2	5783.9	0.43%	7164.3	7280.8	1.62%	7333.7	7342.0	0.11%
				4245.2	4228.6	-0.39%				7408.7	7359.6	-0.66%			
5	2526.9	2531.7	0.19%	4182.5	4199.2	0.40%	5752.3	5775.5	0.40%	7192.9	7309.6	1.62%	7390.3	7331.9	-0.79%
6	2522.5	2528.1	0.22%	4175.1	4193.2	0.43%	5612.9	5719.0	1.89%	7244.5	7298.8	0.75%	7301.4	7321.8	0.28%
							5862.2	5814.9	-0.81%						

Table 1. Comparison of analytically calculated and numerically simulated cutoff frequencies for all eigenmodes shown in Fig. 2(f) in the main text.

P2. Dispersion relations under different degeneracy-lifting conditions.

Here we will discuss in detail the two conditions in Eq. (S21).

We first discuss Condition 1, assuming that Condition 2 is satisfied. We vary N to investigate the degeneracy feature of the eigenmodes of SWG. The dispersion curves for some lowest eigenmodes of the CWG (as a comparison) and SWGs with $N=1,2,3,4$ are plotted in Fig. S2. The radius r_0 of the CWG and the inner radius r_1 of SWG are both 40mm. The depth of sawtooth grooves is uniformly set as $\delta_0 = r_0 / 20$, and the outer radius is given by $r_2 = r_1 + \delta_0$. The sawtooth angles are $\theta = 70°, 70°, 15°, 45°$ for $N=1,2,3,4$ respectively, which guarantee Condition 2 is satisfied for all exhibited modes.

Firstly, all eigenmodes in CWG with $m>0$ are degenerate, as is shown in Fig. S2(a). When there is only one convex ($N=1$), all degenerate branches split into two, as is shown in Fig. S2(b). This is because for any m, Condition 1 $\frac{2m}{N} = 2m \in \mathbb{Z}$ is always satisfied. The same situation also occurs in $N=2$ (Fig. S2 (c)) where $\frac{2m}{N} = m \in \mathbb{Z}$. When $N=3$ (Fig. S2 (d)), only $(3,0)$ branches split ($\frac{2m}{N} = 2 \in \mathbb{Z}$) while $m=1,2$ branches don't. Likewise, the eigenmodes with $m=6,9,12,...$ will also split. When $N=4$ (Fig. S2 (e)), $(2,0)$ branches split ($\frac{2m}{N} = 1 \in \mathbb{Z}$) while $m=1,3$ branches don't. Likewise, the eigenmodes with $m=4,6,8,...$ will also split.

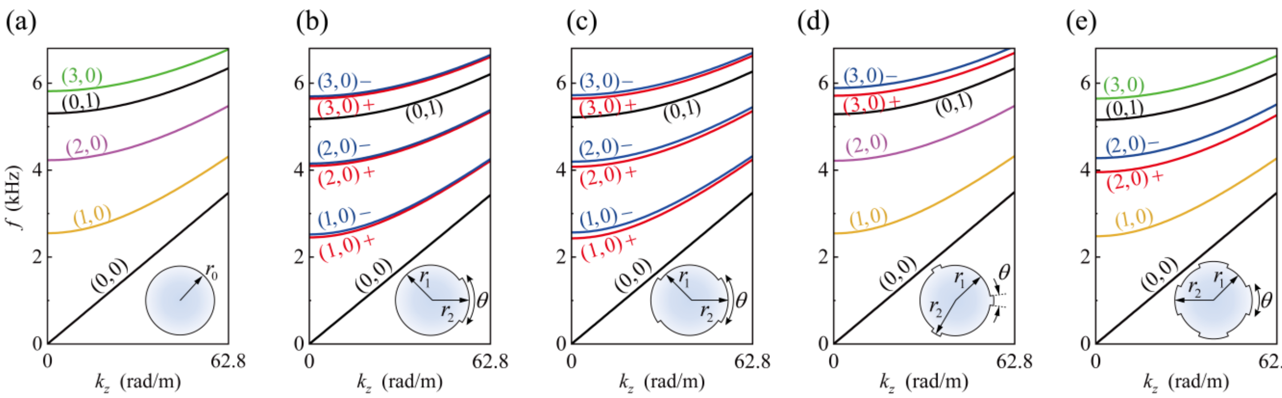

Fig. S2. Dispersion relations of the lowest-order modes in a CWG and SWGs with *N*=1,2,3,4.

Degenerate modes split when satisfying $\frac{2m}{N} \in \mathbb{Z}$. The parameters are: (a) CWG $(r_0 = 40\,\mathrm{mm})$. (b-e) SWG $(r_1 = 40\mathrm{mm}, r_2 = 42\mathrm{mm})$ with number and groove central angle: (b) $N = 1, \theta = 70°$, (c) $N = 2, \theta = 70°$, (d) $N = 3, \theta = 15°$, (e) $N = 4, \theta = 45°$. Insets are the cross-section views.

When Condition 1 has been satisfied, we investigate the degenerate feature of eigenmodes by changing θ. To this end, we choose $N = 2$ as an example and preserve the parameters r_1, r_2, δ_0. The simulated cutoff frequencies of some lowest $m > 0$ eigenmodes with θ varying from 0 to π are exhibited in Fig. S3. It shows that the cutoff frequencies of a pair of eigenmodes with the same order exhibit alternating oscillations and they intersect at some specific points. For instance, the degeneracy between $(1,0)+$ and $(1,0)-$ modes is restored at $\theta = 178.42° \approx \pi$, which agrees well with the degenerate condition $m\theta = \pi$. The cutoff frequencies of $(2,0)+$ and $(2,0)-$ modes converge to the same values at $\theta = 90.15° \approx \pi/2$, $177.84° \approx \pi$, $270.46° \approx 3\pi/2$, where they satisfy $m\theta = \pi, 2\pi, 3\pi$, respectively. $(3,0)+$ and $(3,0)-$ modes intersect at $\theta = 59.24° \approx \frac{\pi}{3}$, $118.96° \approx \frac{2\pi}{3}$, $176.44° \approx \pi$, $239.21° \approx \frac{4\pi}{3}$, $299.41° \approx \frac{5\pi}{3}$, which are all in good agreement with $m\theta \in \pi\mathbb{Z}$. Note there exists a very small error due to the slight distortion of field distributions from the Bessel modal pattern.

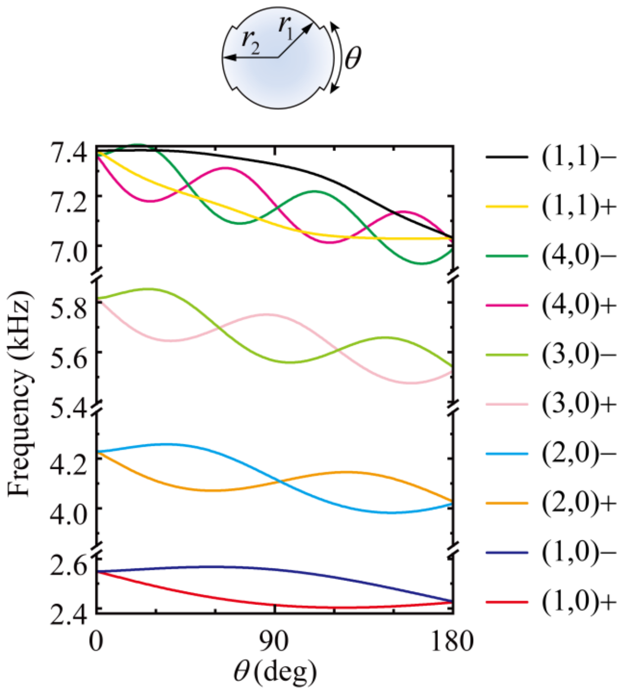

Fig. S3. Numerically simulated SWG cutoff frequencies as a function of the groove central angle. The parameters are $r_1 = 40\text{mm}, r_2 = 42\text{mm}, N = 2$. $(m,n)+$ and $(m,n)-$ stand for a pair of perturbed states, corresponding to 2-fold degenerate state (m,n) in CWG.

P3. Analytical derivation of the acoustic Malus' law in a two-SWG system.

A two-SWG system is constructed by connecting two identical SWGs (labelled as SWG1 and SWG2) with $r_1 = 40\text{mm}, r_2 = 42\text{mm}, \theta = 70°$ and $N = 2$ (identical to Fig. 2(d) in the main text), as is schematically shown in Fig. S4(a). SWG1 is rotated around the central axis ($z-$axis) by an angle $\Delta\varphi$, while SWG2 remains fixed. This relative rotation between two SWGs provides a difference in polarization directions of degeneracy-lifted orbital eigenmodes in SWG1 and SWG2.

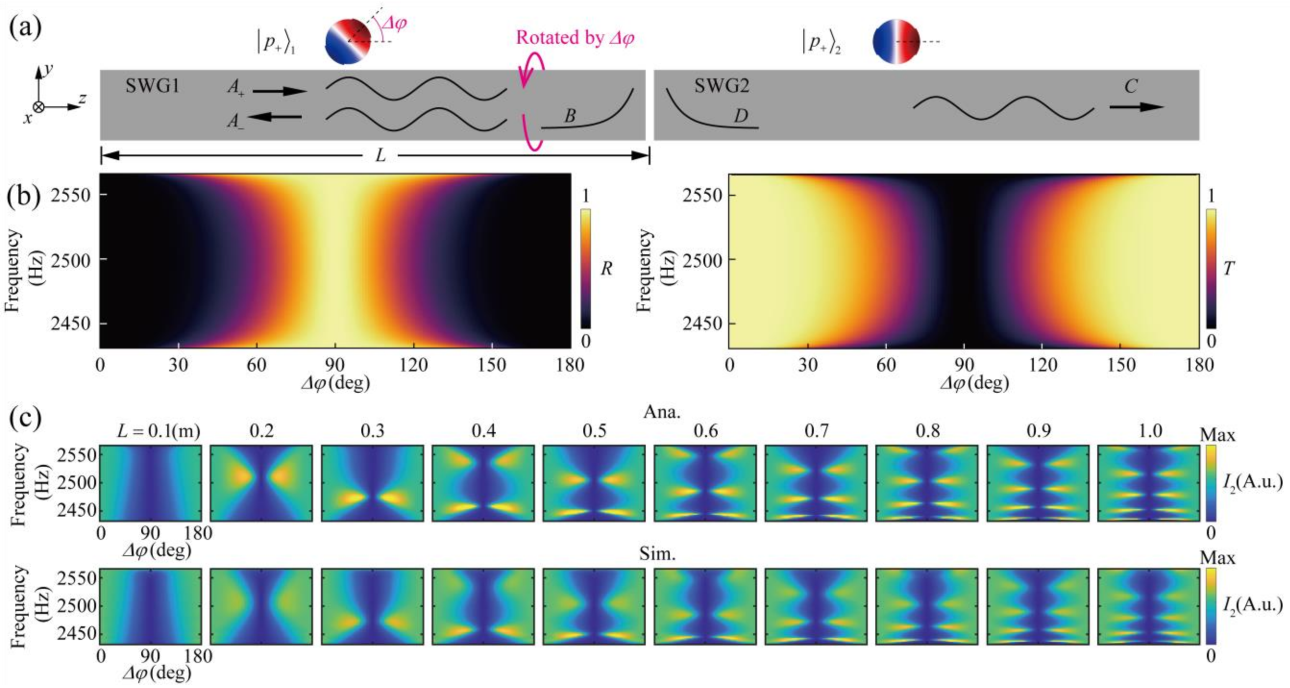

Fig. S4. Rotation-controlled acoustic transmission in the two-SWG system. (a). Schematic illustration of wave scattering on the interface between two SWGs. $\Delta\varphi$ is the angle between two polarization directions of $|p_+\rangle$ modes in SWG1 and SWG2. A_+, A_-, C are amplitudes of propagating $|p_+\rangle$ modes while B, D are the amplitudes of evanescent $|p_-\rangle$ modes. (b) Analytically calculated reflectance R and transmittance T vs. $\Delta\varphi$ and frequency. (c) Analytical (top) and simulated (bottom) transmitted wave intensity in SWG2, obtained by treating SWG1 as a Fabry–Pérot cavity of variable length L.

Since degeneracy-lifting conditions are satisfied, the degenerate modes $(1,0)$ in CWG split into two individual p-orbital modes, represented as $|p_+\rangle$ and $|p_-\rangle$. The cutoff frequencies of $|p_+\rangle$ and $|p_-\rangle$ in this SWG are $f_+ = 2431\text{Hz}$ and $f_- = 2566\text{Hz}$, respectively (be aware that the subscripts $+,-$ denote the angular basis $\{\cos\varphi\},\{\sin\varphi\}$). Hence we set the working frequency between the two cutoff frequencies, i.e., in the range of [2431,2566] Hz, in order to make sure $|p_+\rangle$ is a unique p-orbital channel in both SWGs. Its propagating wavenumber is given by $k_z = \sqrt{k^2 - k_+^2}$, where $k = \frac{2\pi f}{c_0}$ and $k_+ = \frac{2\pi f_+}{c_0}$. On the other hand, $|p_-\rangle$ behaves as an evanescent mode decaying by e^{-Kz}, where $K = \sqrt{k_-^2 - k^2}$ and $k_- = \frac{2\pi f_+}{c_0}$. We can write the p-orbital modes for $\Delta\varphi$-rotated SWG1

$$\begin{aligned} |p_+\rangle_1 &\approx J_1(k_+ r)\cos(\varphi - \Delta\varphi)e^{ik_z z} \\ |p_-\rangle_1 &\approx J_1(k_- r)\sin(\varphi - \Delta\varphi)e^{-Kz} \end{aligned}. \tag{S24}$$

The approximation originates from the eigenfield distortions resulted by the sawtooth grooves. Details of the Bessel function evaluation are provided in Supplementary Material S1 of our previous study [2]. For SWG2

$$\begin{aligned} |p_+\rangle_2 &\approx J_1(k_+ r)\cos\varphi e^{ik_z z} \\ |p_-\rangle_2 &\approx J_1(k_- r)\sin\varphi e^{-Kz} \end{aligned}. \tag{S25}$$

In practice, a dipolar source aligned with the polarization orientation of $|p_+\rangle_1$ is fixed at the leftmost port of SWG1 (embedded in foam, the photo is shown in Fig. 3(a) in the main text) and rotates with SWG1, which guarantees the efficient excitation of $|p_+\rangle_1$. During wave propagation in the two-SWG system, when the incident $|p_+\rangle_1$ mode undergoes scattering at the interface between two SWGs, part of the energy transmits into SWG2, forming forward propagating $|p_+\rangle_2$ mode and also induces evanescent $|p_-\rangle_2$ modes. Owing to the lossless nature of the system, the rest of the energy is fully reflected into the SWG1, in the form of reverse counterparts (towards $-z$ axis) corresponding to propagating mode $|p_+\rangle_1$ and evanescent mode $|p_-\rangle_1$, as illustrated in Fig. S4(a).

The total pressure field in SWG1 can be written as

$$p_1 = \cos(\varphi - \Delta\varphi) J_1(k_+ r)\left(A_+ e^{ik_z z} + A_- e^{-ik_z z}\right) + B\sin(\varphi - \Delta\varphi) J_1(k_- r) e^{Kz}, \tag{S26}$$

where A_+ and A_- are the amplitudes of incident and reflected $|p_+\rangle_1$ component, respectively. B represents the amplitude of the evanescent $|p_-\rangle_1$ component. While the total pressure field in SWG2 can be written as

$$p_2 = CJ_1(k_+ r)\cos(\varphi) e^{ik_z z} + DJ_1(k_- r)\sin(\varphi) e^{-Kz}, \tag{S27}$$

where C and D are the amplitudes of $|p_+\rangle_2$ and $|p_-\rangle_2$, respectively. The leftward-propagating counterpart in SWG2 is eliminated, due to the open boundary condition at the rightmost port of SWG2. The pressure and the normal velocity component $v_z = \frac{1}{i\rho_0\omega}\partial_z p$ must be continuous at the interface between SWG1 and SWG2, which yield

$$\begin{aligned} A_- &= \frac{\left(1-\gamma^2\right)\sin^2\Delta\varphi}{(1-\gamma)^2\sin^2\Delta\varphi + 4\gamma} A_+ \\ B &= \frac{(1-\gamma)\sin 2\Delta\varphi}{(1-\gamma)^2\sin^2\Delta\varphi + 4\gamma} A_+ \\ C &= \frac{4\gamma\cos\Delta\varphi}{(1-\gamma)^2\sin^2\Delta\varphi + 4\gamma} A_+ \\ D &= \frac{2(\gamma+1)\sin\Delta\varphi}{(1-\gamma)^2\sin^2\Delta\varphi + 4\gamma} A_+ \end{aligned}, \tag{S28}$$

where $\gamma = \frac{k_{-,z}}{k_{+,z}} = \frac{iK}{k_z}$. For ease of deriving Eq. (S28), we have utilized an approximation $J_1(k_+ r) \approx J_1(k_- r)$. This approximation is effective as the sawtooth grooves can be considered a perturbation, causing no significant distortion to the radial Bessel pattern [2]. Then the reflection and transmission coefficients can be obtained as

$$\begin{aligned} r(\Delta\varphi) &= \frac{A_-}{A_+} = \frac{\left(1-\gamma^2\right)\sin^2\Delta\varphi}{(1-\gamma)^2\sin^2\Delta\varphi + 4\gamma} \\ t(\Delta\varphi) &= \frac{C}{A_+} = \frac{4\gamma\cos\Delta\varphi}{(1-\gamma)^2\sin^2\Delta\varphi + 4\gamma} \end{aligned}. \tag{S29}$$

Function $t(\Delta\varphi)$ can be regarded as the acoustic Malus' law in this two-SWG system. It is naturally more complicated than the conventional $\cos\Delta\varphi$- dependent Malus' law. The difference is that the light component perpendicularly polarized to the polarizer is discarded due to the full absorption. However, in our acoustic waveguide system, the perpendicularly polarized *p*-orbital component will encounter multiple scattering processes. The transmittance and reflectance, i.e., $T=|t|^2$ and $R=|r|^2$, as shown in Fig. S4(b), depend on both $\Delta\varphi$ and frequency, obeying the relation $T+R=1$. Despite a complicated $\Delta\varphi$-dependence, acoustic transmittance equals 1 at $\Delta\varphi=0°$, then gradually decreases as $\Delta\varphi$ increases to $90°$ and eventually vanishes at $\Delta\varphi=90°$.

Eq. (S29) has revealed the scattering characteristics of a *p*-orbital mode at the interface of the two-SWG system. However, in the experiment, the leftmost port of SWG1 is sealed by a foam layer, then the acoustic wave will also be reflected by the foam layer. The foam layer with a flat surface whose characteristic impedance is very close to that of air, given by $Z_c=\rho_0 c_0$. For a $m>0$ order incident wave mode (equivalent to an oblique incident plane wave), the normal specific acoustic impedance at the port is given by [3]

$$Z_n=\frac{p}{\vec{v}\cdot\vec{n}}=\frac{p}{v_z}=\frac{\rho_0\omega}{k_z}. \tag{S30}$$

The reflection coefficient at the leftmost port caused by the scattering of the foam is given by

$$r_s=\frac{Z_c-Z_n}{Z_c+Z_n}=\frac{\frac{1}{k}-\frac{1}{k_z}}{\frac{1}{k}+\frac{1}{k_z}}=\frac{k_z-k}{k_z+k}. \tag{S31}$$

The acoustic wave will undergo infinite reflections at the leftmost port of SWG1 and the interface between SWG1 and SWG2. Applying infinite reflections, the intensity in SWG1 can be written as [4]

$$I_1=\frac{1}{\left|1-rr_s e^{i2k_zL}\right|^2}. \tag{S32}$$

By using the acoustic Malus' law in Eq. (S29), the transmitted wave intensity in SWG2 is given by

$$I_2=T\cdot I_1=\frac{T}{\left|1-rr_s e^{i2k_zL}\right|^2}. \tag{S33}$$

When $\Delta\varphi=90°$, it yields $T=0$ and further $I_2=0$, meaning the wave intensity in SWG2 completely vanishes. We verify Eq. (S33) by comparing the transmitted intensity of analytical calculation with that of numerical simulation and their results match very well, as is shown in Fig. S4(c).

P4. Analysis of *p*-orbital BICs using the effective square-well model.

A *p*-orbital BIC is generated in a three-SWG system. The middle SWG with length L acts as a resonator, while the other two outer SWGs, each with length L_s, are placed axially on both sides and play the role of open channels. By setting the groove orientation of the middle SWG orthogonal to that of the two outer SWGs, this system can be regarded as an effective finite-depth square well model. A general principle for realizing a *p*-orbital BIC is to confine the $|p_+\rangle$ mode in the well (SWG2) using SWG1 and SWG3 as barriers. Utilizing frequency selectivity (by setting $k_+ < k < k_-$), $|p_+\rangle$ mode is the unique allowed *p*-orbital mode with a real axial wavenumber, whereas the $|p_-\rangle$ mode remains evanescent with an imaginary axial wavenumber. The $|p_+\rangle_2$ mode can only couple to the evanescent modes $|p_-\rangle_1, |p_-\rangle_3$ because their modal polarizations align. Therefore, the wave equations along the z-direction in this three-SWG system can be written as

$$\frac{\partial^2 p}{\partial z^2} + (k^2 - k_{\text{cutoff}}^2) p = 0, \tag{S34}$$

where $k = \dfrac{2\pi f}{c_0}$, and k_{cutoff} represents the effective cutoff wavenumber, defined by

$$k_{\text{cutoff}} = \begin{cases} k_+, & z \in [-L/2, L/2] \\ k_-, & \text{otherwise} \end{cases}. \tag{S35}$$

Mathematically, Eq. (S34) is equivalent to a one-dimensional stationary Schrödinger equation for a square finite-depth potential well along the *z*-axis. From a perspective of formal analogy, k^2 mimics the particle energy and $k_+^2 - k_-^2$ defines an effective potential barrier experienced by $|p_+\rangle$ modes, as shown in Fig. S5(a). Here, we utilize the approximation $J_1(k_- r) \approx J_1(k_+ r)$ because ignoring their difference does not cause significant change but only brings a minor error to conclusions [2].

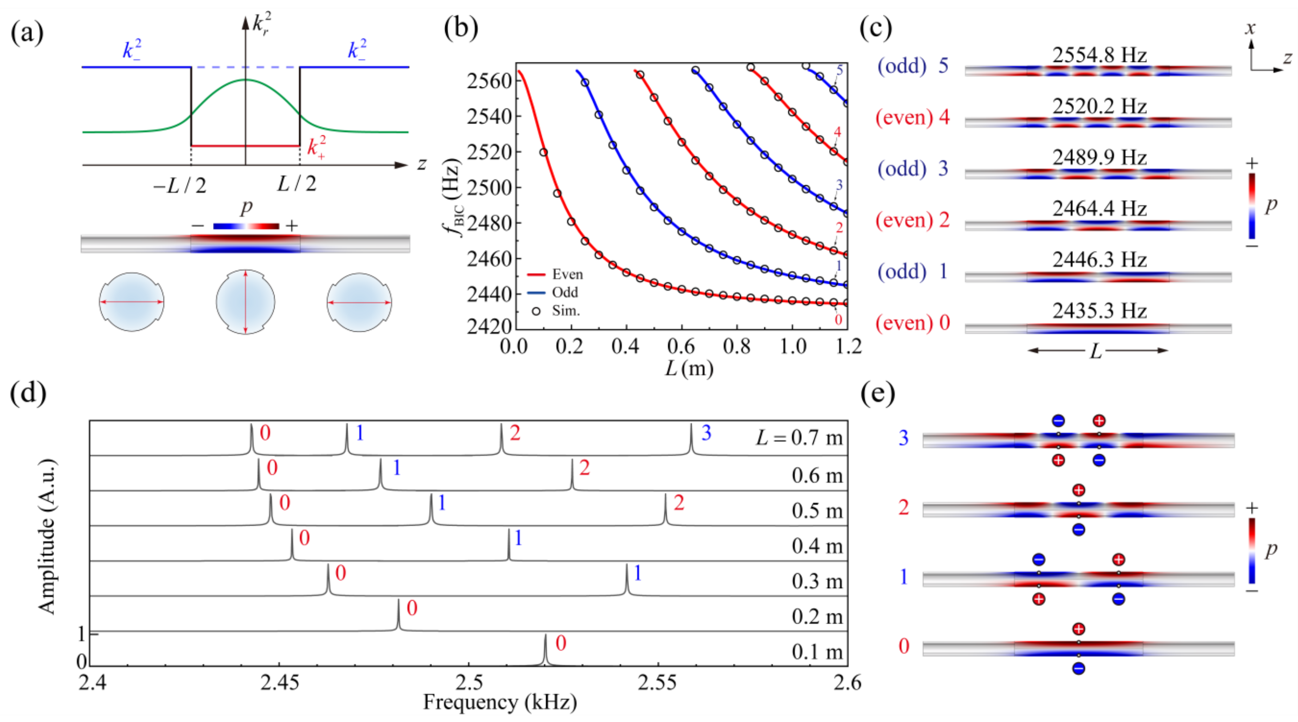

Fig. S5 Bound states of the one-dimensional effective square well in the three-SWG system (a) Scheme of the effective square potential well for *p*-orbital-mode dynamics when $|p_+\rangle_1 \perp |p_+\rangle_2 \perp |p_+\rangle_3$ in three-SWG structure. The geometric parameters of SWG are identical to those in Fig. (4) in main text. k_r represents the effective transverse cutoff wavenumber in SWGs for *p*-orbital modes with the same angular function as $|p_+\rangle_2$. $k_+ = 43.9\mathrm{rad/m}$ and $k_- = 46.3\mathrm{rad/m}$ correspond to the lower and upper cutoff wavenumber of the degeneracy-lifted *p*-orbital eigenmodes, respectively, corresponding to cutoff frequency 2431Hz and 2566Hz, respectively. $k_-^2 - k_+^2$ can be mimicked as the depth of well. If $k_+ < k < k_-$, the $|p_+\rangle_2$ mode will be confined in the middle SWG, analogous to a particle bound in a finite square well. (b) Resonant frequencies of *p*-orbital BICs dependent on the length of middle SWG L. Red (Blue) curves represent analytically solved results of even (odd) states while black circles represent numerically simulated results. (c) Modal field distributions of *p*-orbital BICs corresponding to different orders in (b). The SWG2 length is chosen by $L = 1.15\mathrm{m}$ for illustration. (d) The wave amplitudes in the middle SWG versus different L, where the number notations of resonance peaks correspond to the order in (c). (e) The diagram of source settings for exciting BICs, positions determined by field nodes, with $L = 0.7\mathrm{m}$ for illustration.

The solution of Eq. (S34) in the middle SWG can be expressed as

$$p = J_1(k_+ r)\left(A_+ e^{ik_z z} + A_- e^{-ik_z z}\right), \tag{S36}$$

where A_+ and A_- represent the amplitudes of forward and backward propagation waves, respectively. $k_z = \sqrt{k^2 - k_+^2}\,(k_+ < k)$ indicates the propagating wavenumber of $|p_+\rangle$ mode. In the two outer SWGs, the solutions are evanescent away from the interface between middle SWG and outer SWGs, expressed as

$$p = \begin{cases} B_+ J_1(k_- r) e^{-Kz}, & z > L/2 \\ B_- J_1(k_- r) e^{+Kz}, & z < -L/2 \end{cases}, \tag{S37}$$

where B_+ and B_- represent the amplitudes. $K = \sqrt{k_-^2 - k^2}$ represents the decaying factor. It requires that both p and $\frac{\partial p}{\partial z}$ are continuous at $z = \pm\frac{L}{2}$, which can be written in the matrix form

$$MX = 0, \tag{S38}$$

where

$$M = \begin{pmatrix} e^{ik_z\frac{L}{2}} & e^{-ik_z\frac{L}{2}} & -e^{-K\frac{L}{2}} & 0 \\ ik_z e^{ik_z\frac{L}{2}} & -ik_z e^{-ik_z\frac{L}{2}} & Ke^{-K\frac{L}{2}} & 0 \\ e^{-ik_z\frac{L}{2}} & e^{ik_z\frac{L}{2}} & 0 & -e^{-K\frac{L}{2}} \\ ik_z e^{-ik_z\frac{L}{2}} & -ik_z e^{ik_z\frac{L}{2}} & 0 & -Ke^{-K\frac{L}{2}} \end{pmatrix}, \quad X = \begin{pmatrix} A_+ \\ A_- \\ B_+ \\ B_- \end{pmatrix}. \tag{S39}$$

Nonzero solution requires $|M| = 0$, which yields

$$\left(K^2 - k_z^{\,2}\right)\sin\left(k_z L\right) + 2Kk_z\cos\left(k_z L\right) = 0. \tag{S40}$$

It can be solved numerically. Once the roots are obtained, denoted by k_{BIC}, we can get the resonance frequency of *p*-orbital BICs simply by

$$f_{\mathrm{BIC}} = \frac{c_0 k_{\mathrm{BIC}}}{2\pi}. \tag{S41}$$

The analytical results obtained from Eq. (S40) and simulation results are in excellent agreement, as is shown in Fig. S5(b). As *L* increases, Eq. (S40) has more solutions, therefore one can observe that the available number of *p*-orbital BICs increases as the well width grows. In addition, the frequencies of the same order *p*-orbital BICs can be observed to decline as the well width grows because they have a longer effective wavelength along the z-direction. In principle, no matter how small L is, there always exists at least one *p*-orbital BIC, sharing a common conclusion with the potential well model in the quantum mechanics [5].

For a better understanding of *p*-orbital high-order BICs, we choose $L = 1.15\mathrm{m}$ as an example to reveal the pressure field distributions of BICs, as is shown in Fig. S5(c). As can be observed, all these *p*-orbital BICs exhibit common dipole patterns in the cross section. On the other hand, they can be classified as even- and odd-parity states with respect to the z direction. Here, the order of a *p*-orbital BIC is determined by the number of modal nodes along *z*-direction. An even (odd) number of axial nodes corresponds to even (odd) parity. The 0th order *p*-orbital BIC exists for any well width and any nonzero well depth, equivalent to the ground state of a bound particle in a square well. l-th ($l > 0$) order *p*-orbital BIC can be considered as the l-th excited state. The higher the order of a *p*-orbital BIC, the smaller the decaying factor of the evanescent state, leading to a deeper penetration in outer SWGs. It should be noted that the BIC does not form a standing wave in the middle SWG, because the depth of well is finite rather than infinite.

Fig. S5(d) shows the wave amplitudes in the middle SWG of a finite-length three-SWG structure excited by dipole sources. The sharp peaks denote the quasi-BIC resonances. A dipolar source placed at the center of SWG2 can excite even-parity *p*-orbital quasi-BICs, which is experimentally demonstrated in the main text. However, the center-placed dipolar source cannot excite odd-parity states, because the field at the center of SWG2 is zero. Hence, in order to observe the odd-parity *p*-orbital BICs, we should carefully arrange the locations of dipolar sources. As shown in Fig. S5(e), when $L = 0.7\mathrm{m}$, we use two pairs of dipolar sources instead of one pair to excite the odd-parity BIC. They are placed correspondingly at the two pairs of antinodes, which are mirror-symmetric with respect to the center of SWG2 and anti-phased. Obviously, the 1st and 3rd odd-parity *p*-orbital BICs have been successfully excited. Since the odd-parity BICs of different orders differ in the z position of their antinodes, the positions of these dipolar sources are correspondingly adjusted so that they are strictly set at these antinodes, thereby ensuring effective excitations of the corresponding odd-parity BICs.

P5. Analysis of the exponential dependence of the BIC Q factor on the barrier width.

In a practical three-SWG system, the finite lengths of two outer SWGs will affect the Q factor of BIC. To quantitatively illustrate how Q factor depends on the length of outer SWGs, we perform an analysis by investigating the energy leakage of the sound waves in our open system. Considering the eigensolution in the one-dimensional square well along z-direction, the temporal sound energy density is

$$\mathcal{E}=\frac{1}{2}\rho_0 v_z^2+\frac{p^2}{2\rho_0 c_0^2}, \tag{S42}$$

where

$$v_z=\frac{ik_z p}{\omega\rho_0}. \tag{S43}$$

Assuming the eigenfrequency is complex, the harmonic total energy can be expressed as

$$W=W_0 e^{i\omega t}=W_0 e^{i(\omega_r+\omega_i i)t}=W_0 e^{i\omega_r t}e^{-\omega_i t}, \tag{S44}$$

where W_0 is the temporal total energy at the initial state, defined by

$$W_0=\iiint \mathcal{E}\mathrm{dV}. \tag{S45}$$

In Eq. (S44), ω_r and ω_i represent the real and imaginary parts of angular frequency, respectively. Obviously, the existence of the imaginary part of the complex frequency leads to the decaying factor $e^{-\omega_i t}$, indicating the leakage of energy.

More relevantly, we consider how the time-averaged total energy decays with time,

$$\overline{W}=\overline{W_0}e^{-\omega_i t}, \tag{S46}$$

where the time-averaged $\overline{W_0}$ originates from the integral of time-averaged energy density $\overline{\mathcal{E}}$ of the entire system

$$\overline{W_0}=\iiint \overline{\mathcal{E}}\mathrm{dV}, \tag{S47}$$

with

$$\overline{\mathcal{E}} = \frac{|p|^2}{2\rho_0 c_0^2}. \tag{S48}$$

In terms of the conservation of energy, the decay of time-averaged energy equals the radiation of the sound wave that flows out of the system induced by the open boundary condition (OBC)

$$\frac{\mathrm{d}\overline{W}}{\mathrm{d}t} = -\omega_i \overline{W} = -P_{\mathrm{rad}}, \tag{S49}$$

where the power of the radiation P_{rad} is defined by

$$P_{\mathrm{rad}} = \iint_{\mathrm{OBC}} \overline{\eta_z} \mathrm{dS}. \tag{S50}$$

$\overline{\eta_z}$ is the time-averaged energy flux density

$$\overline{\eta_z} = \frac{1}{2}\mathrm{Re}(p \cdot v_z^*) = \frac{1}{2}|p|^2 \mathrm{Re}(\frac{1}{Z_n}), \tag{S51}$$

where Z_n is the normal acoustic impedance of the radiative modes. In the simulation of the bound state, we have set the outer ends of the SWGs as the plane-wave radiation boundaries, mimicking boundaries surrounded by air. Here in the analysis, the impedance of the OBC is considered the characteristic impedance of the air, defined by

$$Z_n = Z_c = \rho_0 c_0 \tag{S52}$$

Note that this impedance is different from Eq. (S30) because here the open channels that bring the energy out of the system have been assumed as plane-wave modes rather than dipolar guided modes. By combining Eqs. (S47)-(S52) and substituting Eq. (S37), we obtain

$$\omega_i = \frac{P_{\mathrm{rad}}}{\overline{W_0}} = \frac{\iint_{\mathrm{OBC}} \frac{1}{2}|p|^2 \mathrm{Re}(\frac{1}{Z_n})\mathrm{d}S}{\iiint \frac{1}{2\rho_0 c_0^2}|p|^2 \mathrm{d}V} = \left(|B_+|^2 + |B_-|^2\right) c_0 e^{-2K(\frac{L}{2}+L_s)}. \tag{S53}$$

Note that the open boundary is at $z = \pm(\frac{L}{2} + L_s)$. For the sake of simplicity in the analysis, we utilize the parity conservation and require $|B_+| = |B_-| = B$, and obtain

$$\omega_i = 2c_0 B^2 e^{-2K(\frac{L}{2}+L_s)}. \tag{S54}$$

Eventually, utilizing the definition of the Q factor, we can obtain

$$Q = \frac{\omega_r}{2\omega_i} = \frac{k_{\mathrm{BIC}}}{4B^2} e^{2K(\frac{L}{2}+L_s)} \propto e^{2KL_s} , \tag{S55}$$

This result proves that the Q factor is proportional to e^{2KL_s}.

References

[1] Y. Long, D. Zhang, C. Yang, J. Ge, H. Chen, and J. Ren, Realization of acoustic spin transport in metasurface waveguides, Nat. Commun. **11**, 4716 (2020).

[2] Z. Song, S. Xie, H. Ding, F. Cai, Y. Peng, X. Zhu, Y. Li, and D. Zhao, Acoustic vortex in a waveguide with a chiral gradient sawtooth metasurface, Phys. Rev. Applied **21**, 064006 (2024).

[3] L. E. Kinsler, A. R. Frey, A. B. Coppens, and J. V. Sanders, *Fundamentals of Acoustics* (John Wiley & Sons, 2000).

[4] N. Ismail, C. C. Kores, D. Geskus, and M. Pollnau, Fabry-Pérot resonator: spectral line shapes, generic and related Airy distributions, linewidths, finesses, and performance at low or frequency-dependent reflectivity, Opt. Express, OE **24**, 16366 (2016).

[5] J. Binney and D. Skinner, *The Physics of Quantum Mechanics* (Oxford University Press, 2014).